Supplementary Information

Maruthamuthu et al. 10.1073/pnas.1011123108

SI Materials and Methods

Experimental Procedure. ***Cell culture.*** Madin–Darby canine kidney (MDCK) G II cells stably expressing GFP-E-cadherin (1) were a gift from James Nelson (Stanford University, Palo Alto, CA). These cells were grown under 5% CO_2 in low glucose DMEM (Gibco) with 1 g/L sodium bicarbonate (Fisher Scientific), penicillin-streptomycin (Gibco), and 10% FBS (HyClone). MDCK cells expressing GFP-vinculin were a gift from Karl Matlin (University of Chicago, Chicago, IL) and were grown in DMEM with 5% FBS and antibiotics. Transfection with plasmid DNA encoding mApple-actin (gift from Mike Davidson, Florida State University, Tallahassee, FL) was performed using Neon (Invitrogen) electroporation system according to the manufacturer's instructions. For traction force microscopy (TFM) experiments, the cells were trypsinized, suspended as single cells, and approximately 10^5 cells were plated in a 60-mm dish containing the coverslip with the polyacrylamide (PAA) gel approximately 20 h before the experiment.

Immunofluorescence. Immunostaining was performed as previously described (2). Briefly, cells were fixed with 1.8% paraformaldehyde in PBS, blocked with 1.5% BSA in PBS, and all antibody incubation steps were done in the presence of 0.5% BSA. Antibodies used were rabbit anti-NMM II A (and B) α-heavy chain (Covance) and rabbit antipaxillin (Santa Cruz Biotech). Fluorophore-conjugated phalloidin was used to stain actin in all immunofluorescence experiments.

PAA substrates for traction force microscopy. PAA gels covalently attached to coverslips were prepared as described previously for traction force microscopy (3). Acrylamide/bis-acrylamide concentrations of 7.5%/0.1% and 7.5%/0.25% were used to prepare PAA gels of nominal Young's moduli 8.4 kPa and 20.7 kPa, respectively (4). We confirmed the gel stiffness with a Bohlin Gemini HRnano (Malvern Instruments) rheometer in a parallel plate geometry (plate gap 500 μm, frequency 1 Hz) and found that gels allowed to polymerize for a duration of 20 min had a Young's modulus of 8.4 ± 0.9 kPa for acrylamide/bis-acrylamide ratio 7.5%/0.1% and 20.1 ± 4.5 kPa for acrylamide/bis-acrylamide ratio 7.5%/0.25%.

The PAA gels contained 40-nm far red beads (Invitrogen) to serve as fiduciary markers for displacement in the gel. Collagen I (BD Biosciences) or fibronectin (Sigma) were chemically cross-linked to the PAA gel surface by using the bifunctional cross-linker sulfo-SANPAH (Pierce). After coupling the sulfo-SANPAH to the PAA gel surface with a 12-mg/mL solution under 254-nm UV light at 1 J/cm^2 for 1.5 min, the surface was rinsed with water and then collagen I or fibronectin was coupled to the surface at 0.2 and 1 mg/mL, respectively, at 4 °C overnight. Unless otherwise specified, traction force data were obtained from cells plated on 8.4-kPa PAA gels coated with collagen I.

Live cell imaging. Imaging was performed with a multispectral spinning disc confocal microscope with a Ti-E microscope body (Nikon), 60× 1.2 NA Plan Apo WI objective (Nikon), CSU-X confocal scanner (Yokogawa), and a HQ2 cooled CCD camera (Roper Scientific) controlled with Metamorph software (MDS Analytical Technologies). For TFM, PAA gel coverslips were mounted in cell culture medium with 10 mM Hepes into a perfusion chamber and imaged at ∼37 °C. Trypsin (0.05%, GIBCO) was perfused at the end of the experiment to detach cells and to obtain bead reference images.

Traction force microscopy. High-resolution traction force microscopy was performed using experimental and computational methods identical to those described previously (3). The details of the methods, including sources of error, are described below:

Bead displacement analysis. Images of fluorescent beads embedded in the PAA gel were obtained with and without the cell adhered and were aligned in a cell-free region by cross-correlation to correct for experimental drift (3). Bead displacements at the gel surface were <10% of the PAA gel thickness. Displacement vectors of the gel were then calculated using particle imaging velocimetry (MATLAB code available at http://www.oceanwave.jp/softwares/mpiv/), filtered, and interpolated using the kriging method to generate displacements on a regular grid with grid sizes of 0.86, 1.72, or 3.44 μm.

Because the initial registration of the two bead images only occurs to pixel accuracy, the subpixel shift was determined from the mean bead displacement over the whole field of analysis (>2,000 μm^2 area). This value was then subtracted from the displacement field in order to obtain the displacement field that is aligned at a subpixel level. This was done only when justified, i.e., with the datasets (approximately 70% of all datasets) wherein no part of the strain field from any other cell (other than the cell of interest) was present within the boundaries of the field of analysis. For the other datasets, wherein an external cell's strain field extended into the boundary of the field of analysis containing the cell of interest, the mean displacement was not set to zero.

Force reconstruction. Given the bead displacement field, the stress field is obtained by considering the substrate as a linear elastic half-space. The solution of the Green's function was obtained using Fourier transform traction cytometry (FTTC) (5) with zeroth-order regularization (6). This traction force reconstruction method has been previously described in detail (3). The mathematical equations for the problem formulation and the method of solution (regularized FTTC) is exactly as implemented in ref. 3. Regularization was employed to obtain robust solutions (6) and has been found to significantly improve FTTC routines (3). The problem is solved in Fourier space and then inverted back to obtain the stress field in real space (3, 6). The traction forces were reconstructed at a grid spacing of 0.86, 1.72, or 3.44 μm. The product of unit grid area and the traction stress vector at that location yields the traction force vector $\vec{T}_i$ at that location.

We have also implemented two previously established methods by which to reconstruct traction stresses, boundary element method (7) and FTTC without regularization (5). We had previously implemented these to test all three methods (3). As described below in *Alternative approaches to reconstruct traction forces*, we find that all three methods yield qualitatively similar results.

Calculation of Total Traction and Cell–Cell Forces. The traction stress field obtained using regularized FTTC is such that the stress exerted at focal adhesions extends over an area larger than the actual adhesion resulting in a larger traction stress "footprint" (8). The integration of all stress vectors within this larger area yields a more accurate measure of the total traction force exerted by the focal adhesion (8). Thus, in order to take into account all the traction exerted by a cell, the traction boundary of the stress footprint is demarcated to delineate the region with cell-generated traction stresses from the region containing only background stresses.

Method to include cell-generated traction. We show that our results are robust with respect to three different methods to demarcate the area over which the traction forces are integrated. An example of each method is shown in Fig. S6.

i. Manual demarcation of above-background traction vectors. The tractions are included with the cell to which they are centripetally oriented. (Fig. S6*B*) This mask can then be progressively dilated or constricted and the sensitivity to these modifications is discussed (Fig. S6 *E*–*G*).
ii. The cell boundary, as detected by GFP-E-cadherin intensity (which is diffusively present all over the cell membrane), is determined. This mask is progressively dilated until all the above-background traction forces are included. (Fig. S6*C*).
iii. A third, "mask-free" option that does not involve constructing a boundary is to simply take into account just the above-median traction forces in the entire analyzed area, which is much larger than the cell pair. This is based on the observation that less than half the traction vectors in the entire analyzed area are above background. A simple linear extrapolation of the cell–cell contact, determined by E-cadherin intensity, is used to divide the analyzed area into two regions, one for each of the cells in the cell pair. All the forces larger than the median force in this region are utilized to calculate the total cellular traction force and the force imbalance is used to calculate the cell–cell force (Fig. S6*D*).

We have shown that all three methods by which a cell boundary is chosen yield qualitatively similar results of the total cell-ECM traction forces and the cell–cell force. For instance, optimized boundaries for method (i) above, applied to the cell pair shown in Fig. S6, yields total cell-ECM force of 469 nN and cell–cell force of 135 nN, whereas the corresponding values obtained by method (ii) above are 461 nN and 134 nN (Fig. S6). In Fig. S7*A*, we show that the cell–cell and cell-ECM forces calculated by the three methods are similar. For example, the forces calculated using the manual and computational mask construction methods above differ on average only by approximately 5%, similar to the uncertainty in the measured cell–cell force. Thus, the results we present here are independent of the method by which the cell-generated traction is included.

In Fig. S6 *F* and *G*, we examine the effect of contracting or dilating the constructed traction boundary used in method (i) above. Constricted boundaries, which result in omission of traction force vectors in the calculation, lead to an overall lower cell–cell force and greater difference between F_{cell1} and F_{cell2}, i.e., higher uncertainty in $F_{\text{cell-cell}}$.

Calculation of traction force imbalance. After choosing the area over which to sum cell-generated traction stress, the sum of the magnitudes of the traction force exerted at each grid point, $\sum|\vec{T}_i|$, yields a measure of the total traction or the total cell-ECM force exerted by the cell. In this work, unless mentioned otherwise, the total cell-ECM traction force for a cell pair is reported on a per cell basis. The vector sum of the traction forces within the boundary $\sum\vec{T}_i$ can be expected to sum to zero for a single cell or a cell island with two or more cells. The minor imbalance that results due to experimental measurement error can be expressed as $|\sum\vec{T}_i|/\sum|\vec{T}_i|$ and is $5\pm3\%$, as quantified in Fig. 1.

Calculation of cell–cell force. The traction force imbalance method, or TFIM, is simply the calculation of cell–cell forces using imbalances in the traction forces. For a cell pair, the vector sum of traction forces $\sum\vec{T}_i$ under cell 1 alone yields the cell–cell force exerted on cell 1 by cell 2, denoted $\vec{F}_{\text{cell1}}$ such that

$$\vec{F}_{\text{cell1}} = \sum_{\text{cell1}}\vec{T}_i.$$

The force exerted on cell 2 by cell 1, $\vec{F}_{\text{cell2}}$, is analogously determined. Because $\vec{F}_{\text{cell1}}$ and $\vec{F}_{\text{cell2}}$ reflect, in theory, two equal and opposite vectors, the average $\vec{F}_{\text{cell-cell}}$ for a cell pair is then calculated as the vector difference: $(\vec{F}_{\text{cell1}}-\vec{F}_{\text{cell2}})/2$.

Calculation of the uncertainty in cell–cell force. For cell pairs, we estimate the uncertainty in the cell–cell force measurement as follows:

1. For each individual cell in a cell pair, we measure the vector sum of traction forces within each cell to obtain $\vec{F}_{\text{cell1}}$ and $\vec{F}_{\text{cell2}}$. Each of these vectors can be considered as the sum of the correct (real) force exerted at the cell–cell contact by its neighbor, $\vec{F}^{\text{ideal}}_{\text{cell1}}$, and the contribution of measurement error, $\Delta\vec{F}_{\text{cell-cell}}$, such that

$$\vec{F}_{\text{cell1}} = \vec{F}^{\text{ideal}}_{\text{cell1}} + \Delta\vec{F}_{\text{cell-cell}}. \qquad \textbf{[S1]}$$

A priori, we would expect the magnitude of error, $|\Delta\vec{F}_{\text{cell-cell}}|$, to be similar for $\vec{F}_{\text{cell1}}$ and $\vec{F}_{\text{cell2}}$. The sum of the force imbalance under each cell is equal to the sum of traction vectors under the entire cell pair such that

$$\vec{F}_{\text{cell1}} + \vec{F}_{\text{cell2}} = \sum_{\text{cell pair}}\vec{T}_i. \qquad \textbf{[S2]}$$

Inserting **S1** into **S2** yields

$$\vec{F}^{\text{ideal}}_{\text{cell1}} + \Delta\vec{F}_{\text{cell-cell}} + \vec{F}^{\text{ideal}}_{\text{cell2}} + \Delta\vec{F}_{\text{cell-cell}} = \sum_{\text{cell pair}}\vec{T}_i. \qquad \textbf{[S3]}$$

Because $\vec{F}^{\text{ideal}}_{\text{cell1}}$ and $\vec{F}^{\text{ideal}}_{\text{cell2}}$ reflect equal and opposite forces, $\vec{F}^{\text{ideal}}_{\text{cell1}} = -\vec{F}^{\text{ideal}}_{\text{cell2}}$, considering the magnitudes of the remaining vectors provides an estimate of the error in the cell–cell force:

$$2|\Delta\vec{F}_{\text{cell-cell}}| \approx \left|\sum_{\text{cell pair}}\vec{T}_i\right|. \qquad \textbf{[S4]}$$

Or,

$$|\Delta\vec{F}_{\text{cell-cell}}| \approx \left|\sum_{\text{cell pair}}\vec{T}_i\right|/2. \qquad \textbf{[S5]}$$

We found that $|\Delta\vec{F}_{\text{cell-cell}}|$ was approximately 10% that of $|\vec{F}_{\text{cell-cell}}|$, providing a measure of the uncertainty of the magnitude of the cell–cell force.
2. The extent of unbalanced traction observed for single cells provides a second estimate of measurement uncertainty of the cell–cell force. Consider the $5\pm3\%$ (maximum, 15%) of unbalanced traction forces measured in individual cells (Fig. 1*C*). For a cell exerting 200 nN of traction, this would result in unbalanced traction of 10 ± 6 nN (maximum, 30 nN). If the direction of this net force imbalance vector occurred away from the cell–cell interface, this would result in an apparent cell–cell force of 10 ± 6 nN (maximum, 30 nN). For a cell exerting traction force of 200 nN, we measure a cell–cell force of 100 nN (Fig. 3*C*). Thus, the measurement uncertainty from error in traction force balance results in average 10% uncertainty of the cell–cell force magnitude (10 nN/100 nN, expressed as a percentage), but the upper bound could be as large as 30% uncertainty (30 nN/100 nN, expressed as a percentage).

For the linear three-cell case, as shown in Fig. 5, the forces exerted by the outer cells on the inner cell were calculated using

TFIM, and equivalent cell–cell forces were assumed to be exerted by the inner cell on the outer cells.

Sensitivity of the forces to displacement and stress grid sizes. Variation of the bead displacement grid size between 0.86 μm and 3.44 μm does not alter the integrated traction force and is shown in Fig. S8. Using a smaller displacement grid size (0.86 or 1.72 μm) altered the total traction force by <4% and the cell–cell force by <1%. Similarly, the calculated cell–cell forces were invariant to changes in the stress grid size from 1–4 μm. Fig. S8 similarly shows invariance of the calculated forces on varying the stress grid size over the same range, while keeping the displacement grid size constant at 3.44 μm. Using a different stress grid size (0.86 or 3.44 μm) altered the total traction force by <7% and the cell–cell force by <3%. All the results presented in this work uniformly used a displacement grid size of 3.44 μm and a stress grid size of 1.72 μm.

Error in single cell/island force balance. Although the magnitude of the vector sum of traction forces exerted by a cell island (single cell or a cell pair) is expected to be zero, various sources of error contribute to this value being a finite, nonzero value. Survey of prior literature (Table S1) shows that previous traction force methods using continuous substrates sometimes impose the condition that traction forces outside the cell are zero and effectively set the vector sum of the traction within the cell boundary to zero in their traction force calculations (5, 9). Apart from such constrained cases, the average error in a complete traction force balance for a single cell ($|\sum \vec{T}_i| / \sum |\vec{T}_i|$) was reported to be approximately 11% on average by Liu et al. (10) using the micropillar substrate method. We find an imbalance of $5 \pm 3\%$ for a single cell or for two cells in a cell pair taken together.

Sources of error. We identified various factors that may contribute to the overall level of accuracy in determination of the total cellular traction force and the cell–cell force:

i. Noise associated with calculation of the bead displacement field appears to be one of the cardinal factors that contributes to error in the total cellular traction force, and therefore to the minor imbalance in the traction forces under a single cell. We determined this contribution in the following manner: For the case of a cell-free region on the gel, we constructed an artificial cell-pair boundary and determined the sum of traction force magnitudes, $\sum |\vec{T}_i|$. We found that this sum was approximately 10 nN. Considering that the traction magnitude sum for a single cell was approximately 250 nN, this translates to approximately 4% error. The calculated cell–cell force for this imaginary cell pair was only about 1 nN, which translates to 1–2% error contribution in the cell–cell force.
ii. Image registration. To obtain subpixel alignment of bead images with and without the cell, the mean displacement over the whole field of analysis was subtracted from the displacement field in order to obtain the displacement field corrected for subpixel alignment. If an external cell was close to the field of analysis, it causes displacements within the field of analysis (but still away from the displacements generated by the cell of interest) and thus the subpixel alignment could not be performed for such data. We estimate that these datasets (approximately 30% of all datasets) had an additional error contribution of approximately 5% or less in the calculated forces, based on comparison between results obtained before and after subpixel correction of displacements for the other datasets. This error contribution can be minimized by analysis of cells that are more than two cell diameters away from neighboring cells.
iii. Boundary artifacts due to spectral leakage are also a problem with FTTC. These have been reported previously (5) and are also sometimes observed in this work and may contribute to the error.

Alternative approaches to reconstruct traction forces. FTTC without regularization (5) and the boundary element method (BEM) (7) are prior well-established methods to reconstruct the traction forces from the displacement field. BEM was implemented as described in ref. 3, and FTTC was implemented exactly as described in ref. 5. We tested whether these alternate methods could recapitulate the direct relationship we observed between the cell–cell and cell-ECM forces, from which all other results follow. Fig. S7*B* shows that both these alternate methods yield similar magnitudes of cell-ECM and cell–cell force. Furthermore, a direct relationship between the cell–cell and cell-ECM force is observed. This reaffirms that the conclusions reached are robust with respect to the method used to reconstruct the traction forces. In fact, the cell–cell force obtained using all three methods (regularized FTTC, FTTC without regularization, and BEM, all using the same means of including cell-generated traction) agree within <5%, as this depends on low spatial frequency of traction variations. It is also worth noting that the total cell-ECM force varies between the different traction reconstruction methods by approximately 10–20%. This may be attributed to overestimation due to noise contributions in FTTC without regularization or due to underestimation in regularized FFTC due to imposed smoothing.

1. Adams CL, Chen Y-T, Smith SJ, Nelson WJ (1998) Mechanisms of epithelial cell–cell adhesion and cell compaction revealed by high-resolution tracking of E-cadherin–green fluorescent protein. *J Cell Biol* 142:1105–1119.
2. Borghi N, et al. (2010) Regulation of cell motile behavior by crosstalk between cadherin- and integrin-mediated adhesions. *Proc Natl Acad Sci USA* 107:13324–13329.
3. Sabass B, Gardel ML, Waterman CM, Schwarz US (2008) High resolution traction force microscopy based on experimental and computational advances. *Biophys J* 94:207–220.
4. Yeung T, et al. (2005) Effects of substrate stiffness on cell morphology, cytoskeletal structure, and adhesion. *Cell Motil Cytoskel* 60:24–34.
5. Butler JP, Tolic-Norrelykke IM, Fabry B, Fredberg JJ (2002) Traction fields, moments, and strain energy that cells exert on their surroundings. *Am J Physiol-Cell Ph* 282:C595–605.
6. Schwarz US, et al. (2002) Calculation of forces at focal adhesions from elastic substrate data: The effect of localized force and the need for regularization. *Biophys J* 83:1380–1394.
7. Dembo M, Wang Y-L (1999) Stresses at the cell-to-substrate interface during locomotion of fibroblasts. *Biophys J* 76:2307–2316.
8. Stricker J, Sabass B, Schwarz US, Gardel ML (2010) Optimization of traction force microscopy for micron-sized focal adhesions. *J Phys Condens Matt* 22:194104.
9. Gaudet C, et al. (2003) Influence of type I collagen surface density on fibroblast spreading, motility, and contractility. *Biophys J* 85:3329–3335.
10. Liu Z, et al. (2010) Mechanical tugging force regulates the size of cell-cell junctions. *Proc Natl Acad Sci USA* 107:9944–9949.

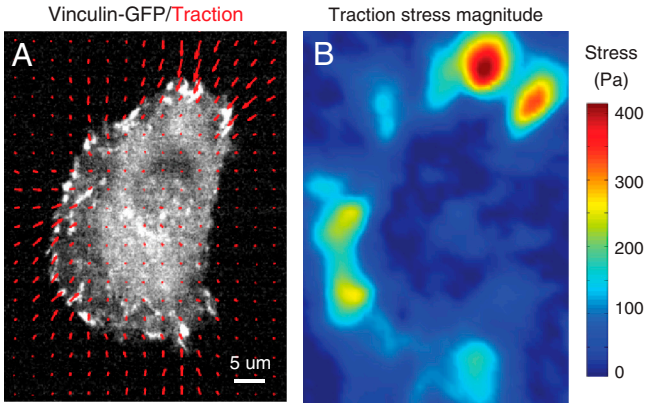

Fig. S1. Single MDCK cell expressing vinculin-GFP on a Cn I, 8.4-kPa gel. (*A*) Vinculin-GFP image of focal adhesions with traction stress vectors superimposed (red). (*B*) Heat scale image of traction stress magnitude of identical cell, with scale bar indicated on the right.

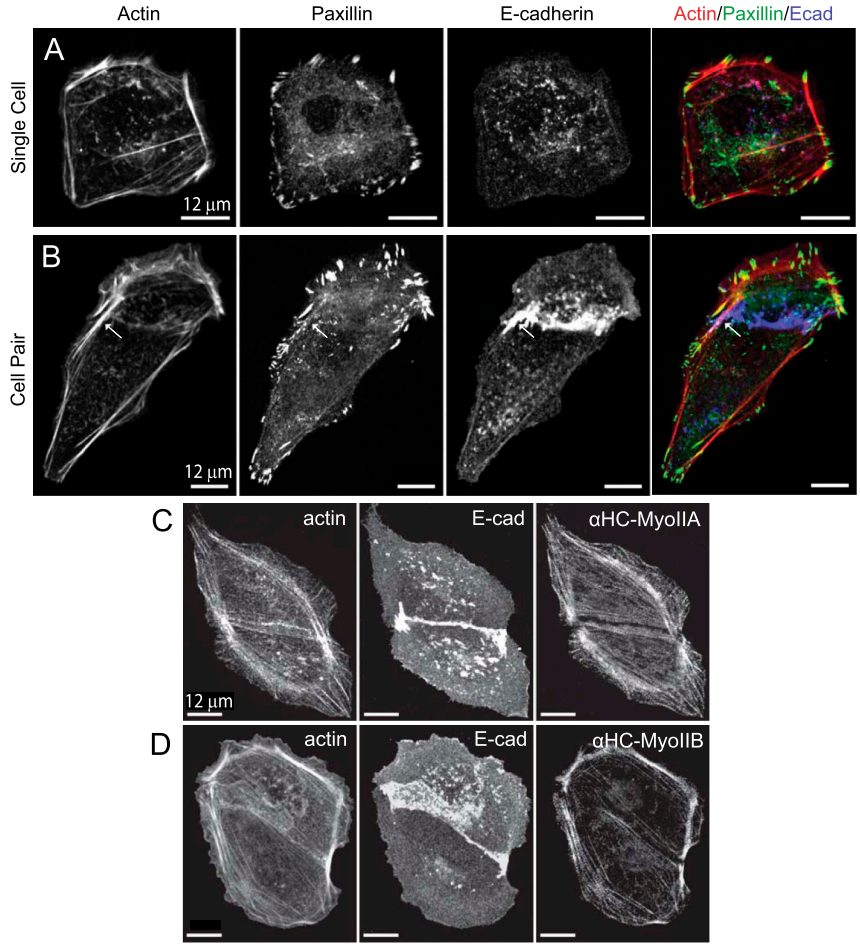

Fig. S2. Actomyosin bundles bridging focal adhesions with each other or with cell–cell adhesions. MDCK cells expressing E-cadherin-GFP and plated on glass coverslips have been fixed and immunostained for paxillin, actin, and/or nonmuscle myosin II. (*A*) In isolated MDCK cells, focal adhesions (FAs) marked by paxillin (green) are interconnected by actin bundles (red). (*B*) In MDCK cell pairs with E-cadherin (blue) localized at the cell–cell contact, actin bundles (red) not only connect paxillin-marked FAs (blue) with each other, but also appear to connect E-cadherin plaques with FAs (white arrow). (*C* and *D*) Localization of nonmuscle myosin II (NMM II) isoforms A and B in MDCK cell pairs. MDCK cell pairs expressing E-cadherin-GFP and plated on glass coverslips were fixed and stained for α-heavy chain of (*C*) NMM II A and (*D*) NMM II B. Note that the NMM II isoforms are conspicuously absent close to the cell–cell contact interface, but are distinctly present in actin bundles ending at the contact edges.

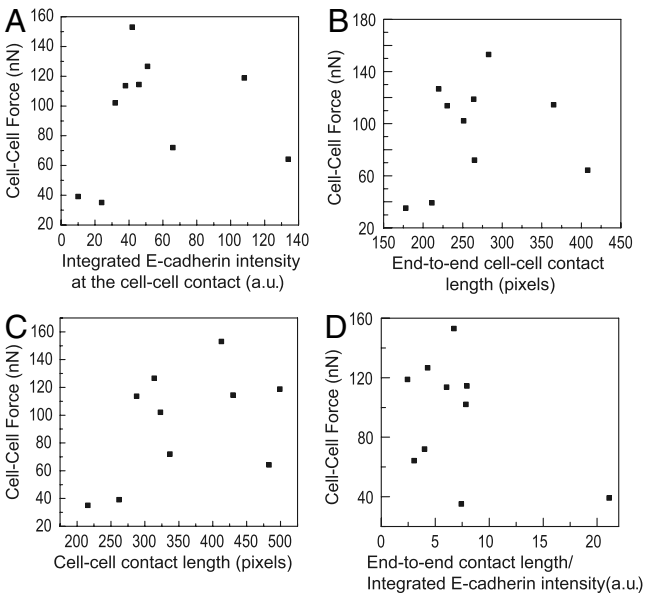

Fig. S3. Endogenous cell–cell force across different MDCK cell pairs is not correlated to the cell–cell contact length or integrated E-cadherin intensity. Endogenous force at cell–cell contacts in MDCK cell pairs plated on Cn I, 8.4–kPa gels versus (*A*) the integrated E-cadherin-GFP intensity at the cell–cell contact, (*B*) projected end-to-end length of the cell–cell contact, (*C*) contour length of the cell–cell contact, and or (*D*) projected end-to-end contact length normalized by the integrated E-cadherin intensity at the interface. The integrated intensity of E-cadherin-GFP at the contact was calculated by taking a z stack of the contact and summing the background subtracted intensities from each plane. Cell–cell contact refers to the contour length of the contact at the plane of maximal E-cadherin localization. Projected end-to-end contact length refers to the length of the straight line joining the extreme points of the cell–cell contact in this plane; this line is also approximately normal to the cell–cell force. No strong correlation is observed in any of the plots *A*–*D*.

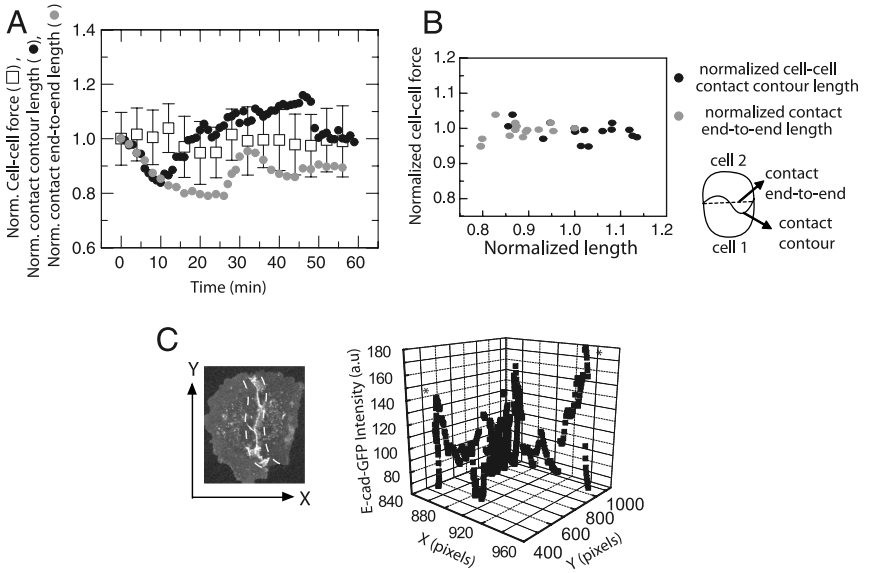

Fig. S4. Endogenous cell–cell force of an MDCK cell pair undergoing random comigration is not correlated to the cell–cell contact length or to the contact end-to-end length. (*A*) Variation of the endogenous cell–cell force (empty squares), cell–cell contact length (black circles), and contact end-to-end length (gray circles) with time, all normalized relative to their initial values, for the MDCK cell pair on a Cn I coated 8.4-kPa PAA gel shown in Fig. 2. The uncertainty in the cell–cell force is represented by the error bars and the uncertainties in the contour, and end-to-end lengths are comparable in dimensions to their circle symbols. (*B*) The normalized cell–cell force as a function of the normalized cell–cell contact contour length (black circles) or end-to-end lengths (gray circles). Schematic below shows the cell–cell contact contour and end-to-end lines. No correlation between the cell–cell force and either measure of the cell–cell contact length is observed, consistent with the data we show in Fig. S3. (*C*) Local maxima in E-cadherin accumulation at the ends of the cell–cell contact in an MDCK cell pair expressing E-cadherin-GFP plated on a Cn I coated 8.4-kPa PAA gel. The E-cadherin intensity (locally integrated perpendicular to the cell–cell contact contour) is plotted as a function of the contour taken to lie on the xy plane.

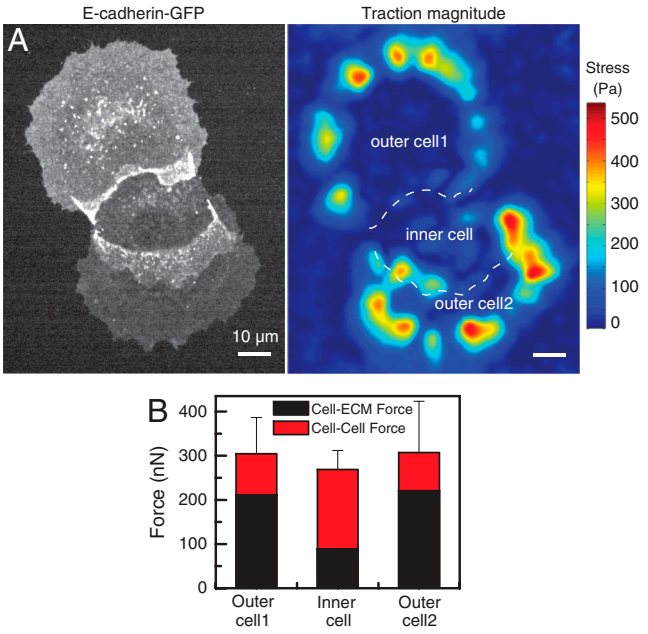

Fig. S5. Three-cell island formed by MDCK cells on a Cn I coated 8.4-kPa PAA gel. (*A*) Example of a three-cell case wherein the inner cell also exhibits appreciable traction, close to the interface with outer cell 2. (*B*) Total cell-ECM and cell-cell force magnitudes exerted by each of the cells. The data represent the average and standard deviation of data from four distinct three-cell islands.

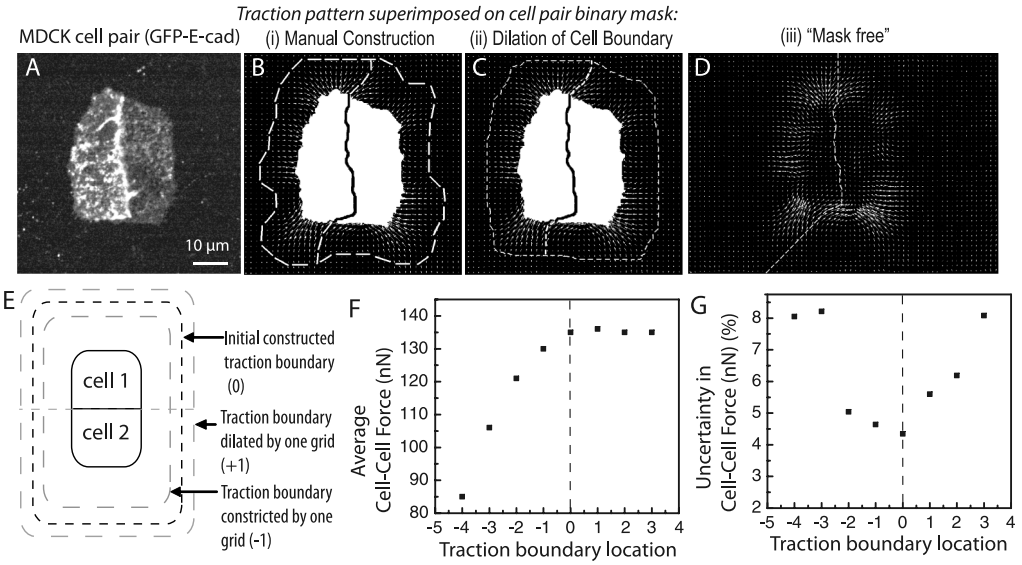

Fig. S6. Construction of cell boundaries used for integration of traction stress vectors. (*A*) MDCK cell pair expressing E-cadherin-GFP and plated on Cn I coated 8.4-kPa PAA gel. (*B* and *C*) Traction forces exerted by the cell pair is shown superimposed on a binary mask of the cell pair. (*B*) Traction boundary constructed manually by inspection by choosing masks sufficiently large to include traction stress vectors above the background and choosing vectors that are centripetally oriented toward the cell center. (*C*) Boundary chosen computationally by identification of the cell perimeter with E-cadherin staining and progressive dilation of the cell boundary to include all the above-background traction is shown as the dashed line. (*D*) Mask/boundary free method of choosing traction stress vectors by drawing lines extending the cell–cell contact and summing up all the traction stress vectors in each region that are above the median value. All three methods of summing traction stresses yield similar magnitudes of cell-ECM traction force and cell–cell force. (*E*–*G*) Traction boundary constructed by manual inspection optimally accounts for all the cell-generated traction forces. (*E*) Schematic showing a cell pair and the constructed traction boundary to include all traction forces of relevance. Constriction (−1, − 2,…) or dilation (+1, + 2,…) of the traction boundary by 1 grid spacing (approximately 2 μm) is also schematically shown. (*F*) The computed average cell–cell force as a function of traction boundary location, in units of constricting (negative) or dilating (positive) the manually chosen traction boundary by one grid spacing. The rapid dropoff of the average cell–cell force with boundary constriction can be explained by the elimination of traction stress vectors upon use of the smaller boundary. (*G*) The uncertainty in the cell–cell force as a function of the traction boundary location. The chosen boundary corresponds to a weak minimum in the uncertainty.

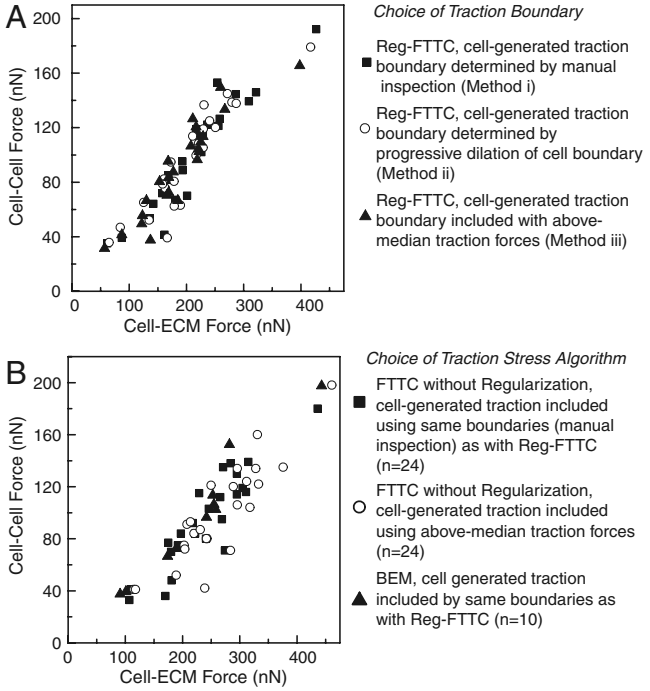

Fig. S7. Direct relationship between cell–cell and cell-ECM forces recapitulated using different methods used to include cell-generated traction and different routines used to reconstruct traction forces. (*A*) Method used to determine boundary of cell-generated traction does not affect the calculation of cell-ECM force or cell–cell force. Plot of the cell–cell force versus the total cell-ECM force per cell for MDCK cell pairs on 8.4-kPa Cn I PAA gels using regularized FTTC. The three different methods used to determine the traction stress vectors used to calculate the cell-ECM force and the cell–cell force for each cell in a cell pair are as follows: (*i*) manual inspection (full squares, $n = 24$), (*ii*) progressive cell boundary dilation (empty circles, $n = 24$), and (*iii*) inclusion of above-median traction stresses in the entire half-plane of the area analyzed determined by the location of the cell–cell contact (full triangles, $n = 24$). The three methods are shown in Fig. S6 and discussed in the *SI Text*. (*B*) Alternative traction force reconstruction methods also yield similar results. The cell–cell force versus the cell-ECM force for a population of MDCK cell pairs on 8.4-kPa Cn I PAA gels as calculated with several different force reconstruction methods. All data shown originate from the image data used to calculate cell-ECM and cell–cell force in Fig. 4*C*, which was performed with regularized FTTC and a manually constructed traction stress boundary. Cell–cell force as a function of cell-ECM force for FFTC without regularization using identical manually constructed traction boundaries used for measurements in Fig. 4*C* (full squares, $n = 24$), BEM using the identical manually constructed traction boundaries used in Fig. 4*C* (filled triangles, $n = 10$), and FTTC without regularization using the boundary free method (*iii*) of integrating all above-median stresses (empty circles, $n = 24$). All methods calculated similar cell-ECM force and cell–cell force and recapitulated the direct relationship between the cell–cell and cell-ECM forces.

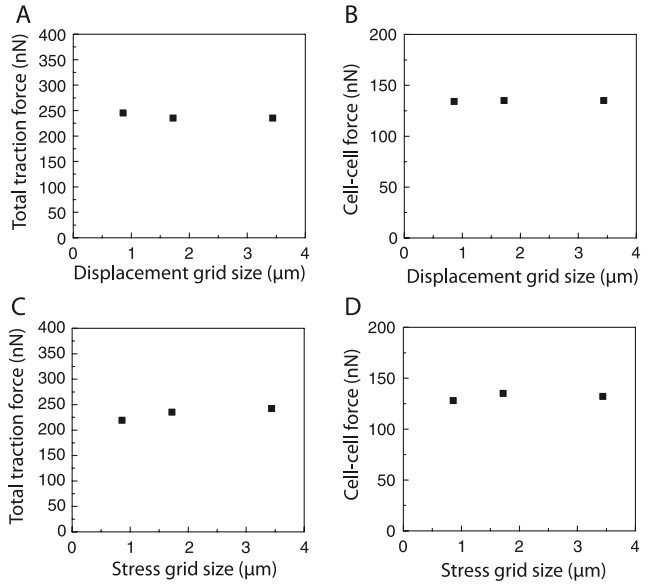

Fig. S8. The grid size of the bead displacement and stress fields do not affect the calculated cell-ECM traction force or the cell–cell force. (*A*) Total cell-ECM traction force as a function of displacement grid size for a constant stress grid size of 1.72 μm. (*B*) Cell–cell force as a function of displacement grid size for a constant stress grid size of 1.72 μm. (*C*) Total cell-ECM traction force as a function of stress grid size for a constant displacement grid size of 3.44 μm. (*D*) Cell–cell force as a function of stress grid size for a constant displacement grid size of 3.44 μm.

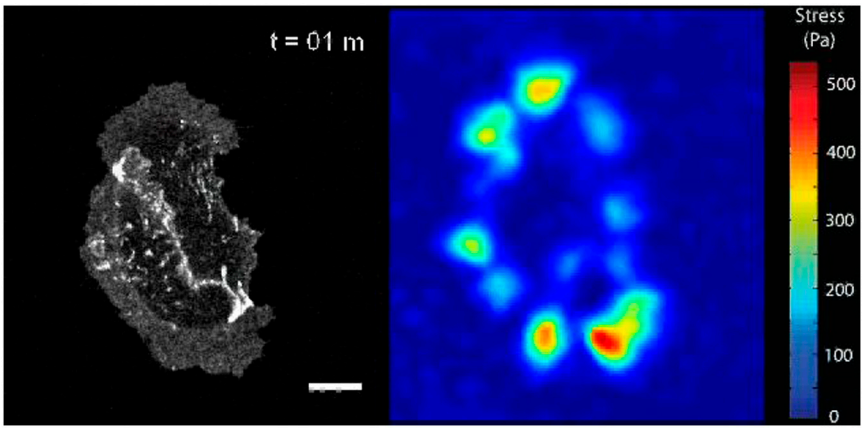

Movie S1. MDCK cell pair expressing E-cadherin-GFP randomly comigrating on a Cn I, 8.4-kPa gel, observed for 1 h. Note changes in both cell shapes as well as in cell–cell contact morphology. The dynamic traction stress heat map of this cell pair is shown on the right.
Movie S1 (TIF)

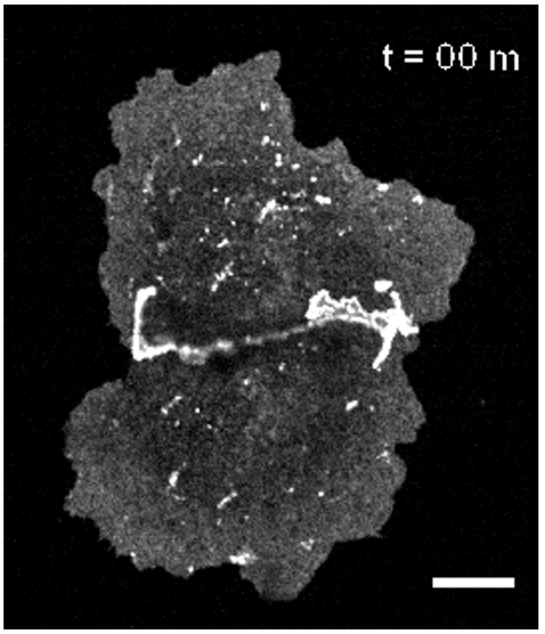

Movie S2. Progressive rupture of the cell–cell contact of an MDCK cell pair (expressing GFP-E-cadherin) during the first approximately 20 min after calcium depletion.
Movie S2 (TIF)

Table S1. Comparison of different traction force microscopy methods and single cell traction force balance reported therein

Reference	Procedure/assumptions	Single cell traction balance
Dembo and Wang (1)	Boussinesq solution for elastic half-space, with regularization, Bayesian likelihood method to solve for tractions	Single cell traction balance not reported.
Butler et al. (2)	Boussinesq solution for elastic half-space, displacements are Fourier transformed, solved for tractions, then inverted back. As part of the procedure, sum of tractions in the entire field of view is set to zero. Two ways of solving: (*i*) Unconstrained FTTC: Tractions not constrained to be within the cell boundary. (*ii*) Constrained FTTC: Tractions outside the cell boundary are set to zero.	Single cell traction balance not reported. (*i*) Contractile moments are reported. Uncertainty in contractile moment due to displacement noise was estimated by borrowing the relation between simulated Gaussian displacement noise and contractile moments and reported to be <1%, but is a conservative estimate as it admittedly disregards contributions from patches of nonzero traction outside the cell. (*ii*) Tractions inside the cell are, in effect, enforced to sum to zero.
Munevar et al. (3); Gaudet et al. (4)	Similar to ref. 1, but with tractions constrained within cell boundary, sum of tractions under the cell set to zero.	Single cell traction balance imposed.
del Alamo et al. (5)	FTTC with finite thickness taken into account.	Complete single cell force balance not reported. Balance of force component along the long axis alone was 4%, reported for $n = 1$ cell.
Sabass et al. (6)	FTTC (using Boussinesq solution) with regularization. Mean displacement over the entire field of analysis is set to zero to aid subpixel alignment, when no other cell's (other than the cell of interest) strain field is present in the field of analysis.	This method is employed in the present paper to evaluate single cell force balances and their statistics.
Liu et al. (7)	Elastic micropillar method, Hooke's law yields force from displacement.	Single cell traction force imbalance is approximately 11% of the sum of the traction force magnitudes.

1. Dembo M, Wang Y-L (1999) Stresses at the cell-to-substrate interface during locomotion of fibroblasts. *Biophys J* 76:2307–2316.
2. Butler JP, et al. (2002) Traction fields, moments, and strain energy that cells exert on their surroundings. *Am J Physiol-Cell Ph* 282:C595–605.
3. Munevar S, Wang Y, Dembo M (2001) Traction force microscopy of migrating normal and H-ras transformed 3T3 fibroblasts. *Biophys J* 80:1744–57.
4. Gaudet C, et al. (2003) Influence of type I collagen surface density on fibroblast spreading, motility, and contractility. *Biophys J* 85:3329–3335.
5. del Álamo JC, et al. (2007) Spatio-temporal analysis of eukaryotic cell motility by improved force cytometry. *Proc Natl Acad Sci USA* 104:13343–13348.
6. Sabass B, et al. (2008) High resolution traction force microscopy based on experimental and computational advances. *Biophys J* 94:207–220.
7. Liu Z, et al. (2010) Mechanical tugging force regulates the size of cell–cell junctions. *Proc Natl Acad Sci USA* 107:9944–9949.